Applied Catalysis B: Environmental 266 (2020) 118650

Contents lists available at ScienceDirect

Applied Catalysis B: Environmental

journal homepage: www.elsevier.com/locate/apcatb

Unravelling the interfacial charge migration pathway at atomic level in 2D/2D interfacial Schottky heterojunction for visible-light-driven molecular oxygen activation

Bisheng Li[a], Shiyu Liu[a], Cui Lai[a,*], Guangming Zeng[a,*], Mingming Zhang[a], Mingzhu Zhou[b], Danlian Huang[a], Lei Qin[a], Xigui Liu[a], Zhongwu Li[c], Ning An[a], Fuhang Xu[a], Huan Yi[a], Yujin Zhang[a], Liang Chen[d]

[a] College of Environmental Science and Engineering, Hunan University and Key Laboratory of Environmental Biology and Pollution Control (Hunan University), Ministry of Education, Changsha, 410082, Hunan, China
[b] Institute of Nanochemistry and Nanobiology, Shanghai University, Shanghai, 200444, China
[c] College of Resources and Environment Science, Hunan Normal University, Changsha, 410082, China
[d] Faculty of Life Science and Technology, Central South University of Forestry and Technology, Changsha, Hunan, 410004, China

ARTICLE INFO

Keywords:
Molecular oxygen activation
2D/2D Schottky heterojunction
Surface charge transfer efficiency
Surface recombination constant
Mechanism

ABSTRACT

Visible-light-driven molecular oxygen activation (MOA) is deemed as the potential route to enhance oxidation capacity of molecular oxygen, while activation efficiency is significantly impeded thanks to the deficient charge carrier separation and transfer. In this work, an atomic scale 2D/2D Schottky heterojunction is prepared using titanium carbide as 2D platform for in situ growth of 2D ultrathin bismuth molybdate nanosheet through anaerobically hydrothermal conditions. This 2D/2D Schottky heterojunction displays high performance for MOA, which is 5.56-fold higher than pristine one. The excellent activation efficiency is originated from ultrahigh charge carrier transfer channel, in which the surface charge transfer efficiency is enhanced (30.73 % vs 18.45 %) and the surface recombination constant is decreased (0.0019 s^{-1} vs 0.0031 s^{-1}) compared to pristine one. The mechanism of photocatalytic MOA is unearthed based on experiment results and various characterizations. This study shows the great potential of atomic scale 2D/2D Schottky heterojunction in photocatalytic MOA.

1. Introduction

Molecular oxygen is regarded as the most green, fertile, and sixpenny oxidizing agent. Unluckily, massive pollutants cannot be directly oxidized by oxygen molecule at mild condition environment because of the spin forbidden reactions [1]. But molecular oxygen can be activated to generate reactive oxygen species (ROS), which is generally recognized as the high-activity oxidant and have been widely employed in environmental chemistry and biochemistry [2–4]. Molecular oxygen activation (MOA) can be achieved through many physical, chemical, and biologic routes [5–7]. Among them, photocatalysis technology for activating molecular oxygen is believed as the most green, sustainable, and inexpensive method. Solar-driven excitonic effects in semiconductor offer numerous photoinduced hot carriers and energies for activating molecular oxygen and producing ROS such as $^{\cdot}O_2^{-}$, $^{\cdot}OH$, $^1O_2$, and H_2O_2, conquering the spin forbidden reaction of the molecular oxygen and promoting its oxidation capacity [8,9]. Thus, unearthing novel photocatalyst with high yields of hot charge carriers is a momentous thing in MOA process.

Among diverse photocatalysts, bismuth based semiconductors, especially the Aurivillius family of Bi_2XO_6 (X=W or Mo) which constructed by alternating $(Bi_2O_2)^{2+}$ and $(XO_4)^{2-}$ perovskite layers, has captured substantial attention owing to their layered structures and superior physicochemical properties [10]. In particular, Bi_2MoO_6 possesses suitable band gap, valence band (VB), and conduction band (CB), which renders it as a prospective photocatalyst. Chen's group has confirmed that Bi_2MoO_6 showed excellent photocatalytic performance for MOA [11]. Unfortunately, the pure bulk Bi_2MoO_6 suffers from the serious photoinduced charge carrier recombination, which undoubtedly impairs its photocatalytic activation efficiency. And recently, Liang and his coworkers prepared monolayer Bi_2MoO_6 by bottom-top hexadecyl trimethyl ammonium bromide (CTAB) assistant hydrothermal route, which showed higher photoactivity than bulk Bi_2MoO_6 owing to the shortened charge carrier transfer distance and exposed active sites [12].

* Corresponding authors.
E-mail addresses: laicui@hnu.edu.cn (C. Lai), zgming@hnu.edu.cn (G. Zeng).

https://doi.org/10.1016/j.apcatb.2020.118650
Received 29 October 2019; Received in revised form 1 January 2020; Accepted 16 January 2020
Available online 17 January 2020

Although charge carrier in monolayer Bi_2MoO_6 can be quickly transferred to catalyst surface, the transferred surface charge carrier still has a tendency to recombine, which still impedes it from practical application.

To restrain the photogenerated charge carrier recombination, various strategies have been employed, which contain doping [13], defect engineering [14], heterojunction construction [15], and carbonaceous materials modification [16]. Among diverse methods, heterojunction construction is indeed verified as a valid strategy. Considering the two-dimensional (2D) structure of monolayer Bi_2MoO_6, unearthing another 2D material to interconnect with monolayer Bi_2MoO_6 could be a better choice. Because 2D/2D heterojunctions possess several superiorities: on the one hand, 2D/2D heterojunctions hold larger interfacial contact area, which significantly expedites interfacial charge carrier separation and migration [17]. On the other hand, 2D/2D heterojunctions usually possess larger specific surface area, which is propitious to mass transfer [18]. In addition, it also holds high photostability owing to the alleviated photocorrosion and agglomeration [19]. Recently, a novel 2D layered transition metal carbides (MXenes) has motivated research upsurge in supercapacitors [20], rechargeable batteries [21], and biosensors [22]. Furthermore, the distinctive properties of Ti_3C_2 MXenes render it as a promising cocatalyst in photocatalytic field: (1) Ti_3C_2 MXenes hold ample hydrophilic functionalities (fluorine, hydroxyl or oxygen groups) on its surface which render it has strong contact with diverse semiconductors [23]; (2) the termination groups with fluorine, hydroxyl or oxygen groups supply numerous active sites [24]; (3) the exposed terminal metal sites (Ti for Ti_3C_2 MXenes) result in higher redox ability compared to conventional carbonaceous materials [25]; (4) the superior electroconductibility of Ti_3C_2 MXenes renders it as an superior electron sink to easily trap photogenerated electron, thereby accelerating photoexcited charge carrier separation and transfer [26]. Qiao et al. also confirmed that Ti_3C_2 MXenes was an excellent cocatalyst by connecting Ti_3C_2 MXenes with CdS for visible-light photocatalytic hydrogen production [27]. In addition, previous studies have revealed that Ti_3C_2 MXenes display metallic property [28,29]. Therefore, combining 2D layered Ti_3C_2 MXenes with monolayer Bi_2MoO_6 is anticipated to form a novel 2D/2D Schottky heterojunction which commonly comes into being between semiconductor and metal interface. Moreover, Schottky heterojunction has been corroborated as high efficacious tactics to expedite photogenerated charge carrier transfer owing to the built-in electric field formed at contact interface between Ti_3C_2 MXenes and monolayer Bi_2MoO_6 [30].

In this study, Bi_2MoO_6/Ti_3C_2 MXene Schottky photocatalyst is successfully prepared by one-step CTAB-assisted anaerobically hydrothermal method. The prepared Bi_2MoO_6/Ti_3C_2 was characterized by various technologies such as X-ray diffraction (XRD), transmission electron microscopy (TEM), and X-ray photoelectron spectroscopy (XPS) to identify the successful preparation. The photocatalytic performance of Bi_2MoO_6/Ti_3C_2 Schottky photocatalyst was evaluated by molecular oxygen activation. The photogenerated electron-hole separation and migration efficiencies were assessed through transient photocurrent (TPC), electrochemical impedance spectroscopy (EIS), and open circuit potential (OCP). In addition, the obtained Bi_2MoO_6/Ti_3C_2 MXene Schottky photocatalyst was also applied to treat river water, lake water, industrial wastewater, and medical wastewater.

2. Materials and methods

2.1. Materials

Bismuth nitrate pentahydrate ($Bi(NO_3)_3{\cdot}5H_2O$), sodiummolybdate dihydrate ($Na_2MoO_4{\cdot}2H_2O$), and CTAB were used as raw material to prepare monolayer Bi_2MoO_6. Ti_3AlC_2 powder was provided by Hello Nano Technology Co., Ltd., Changchun. Hydrochloric acid (HCl) and sodium fluoride (NaF) was used to etch the Ti_3AlC_2 powder. Dmethyl sulfoxide (DMSO) was employed to exfoliate the bulk Ti_3C_2. All chemical reagents are analytical grade and utilized without refining.

In addition, river water was obtained from Xiangjiang River (Changsha, China), lake water was obtained from Taozi lake, (Changsha, China), industrial wastewater was obtained from Hebei Cangzhou Dahua Co., Ltd (China), and medical wastewater was obtained from Changsha 4 st hospital (Changsha, China).

2.2. Synthesis of 2D layered Ti_3C_2 MXenes

The 2D layered Ti_3C_2 MXenes were prepared through etching method coupling with exfoliation procedure [31,32]. Typically, 500 mg of Ti_3AlC_2 ground solid was added into etching solutions which consisted by 80 mmol of NaF and 20 mL of HCl solution (35 %–38 %). The obtained mixture was heated at 60 ℃ for 24 h with constant stir. After that, the bulk Ti_3C_2 was collected through cleaning the mixture with ultrapure water and attenuant HCl solution, and then drying at 80 ℃ for 12 h under vacuum environment. 2D layered Ti_3C_2 MXenes were obtained by exfoliating bulk Ti_3C_2 in DMSO solution. 500 mg of bulk Ti_3C_2 was poured into 10 mL of DMSO solution and stirred at normal atmospheric temperature for 24 h. After that, the obtained mixture was added into 50 mL of ultrapure water and suffered from sonication for several hours. The layered Ti_3C_2 MXenes were obtained through washing, filtration, and drying in vacuum drying oven at 70 ℃ for 12 h (Scheme 1).

2.3. Synthesis of Bi_2MoO_6/Ti_3C_2 MXene Schottky photocatalyst

Bi_2MoO_6/Ti_3C_2 MXene Schottky photocatalyst was synthetized through CTAB-assisted anaerobically hydrothermal method. In a typically procedure, a certain amount of Ti_3C_2 nanosheets were immerged into 40 mL of ultrapure water and underwent sonication for 0.5 h under argon condition to achieve high dispersion. Then, 2 mmol of $Bi(NO_3)_3{\cdot}5H_2O$ was added into aforementioned Ti_3C_2 suspension and stirred for 0.5 h with constant argon aeration. And then another 40 mL of deionized water contained 1 mmol of $Na_2MoO_4{\cdot}2H_2O$ and 300 mg of CTAB were dropwisely appended to $Bi(NO_3)_3{\cdot}5H_2O$ and Ti_3C_2 mixture and were stirred for another 1 h under argon condition. Ultimately, the mixtures were appended to 100 mL Teflon-lined stainless steel autoclave and reacted at 120 ℃ for 24 h. The Bi_2MoO_6/Ti_3C_2 hybrid materials with different mass ratios (0.2 %, 0.5 %, 1 %, and 2 %, Ti_3C_2 to Bi_2MoO_6) were obtained through washing, filtration, and drying (Scheme 1).

2.4. Characterization

The composition of prepared materials was ascertained by XRD using XRD-6100 equipped with Cu-Kα radiation (λ = 0.15418 nm), and the scanning rate was 8° min^{-1} in the 2θ range between 10° and 80° (Japan). The element constitution and valence state of photocatalyst was gained through XPS with Al-Kα X-ray (hν = 1486.6 eV) radiation (ESCALAB 250Xi, America) and binding energy was calibrated with C1 s peaks at 284.80 eV. The morphology and crystal lattice parameter was acquired via TEM and high resolution TEM (HRTEM) (Tecnai G2 F20 S-TWIN TMP). Ultraviolet visible diffuse reflectance spectra (UV–vis DRS) were recorded to test optical property of prepared materials (Varian Cary 300 spectrophotometer). The functional groups of prepared photocatalyst were tested through Fourier transform infrared spectroscopy (FT-IR) (IRTracer-100 FT-IR Spectrometer) in a KBr tablets, scanning from 4000 to 400 cm^{-1} at normal atmospheric temperature. Atomic force microscopy (AFM) was utilized to ascertain thickness of materials (Bruker dimension icon). The reactive oxygen species were tested by electron spin resonance (ESR) employing 5, 5-dimethyl-l-pyrroline N-oxide (DMPO) as a probe on a JES FA200 spectrometer under visible light illumination.

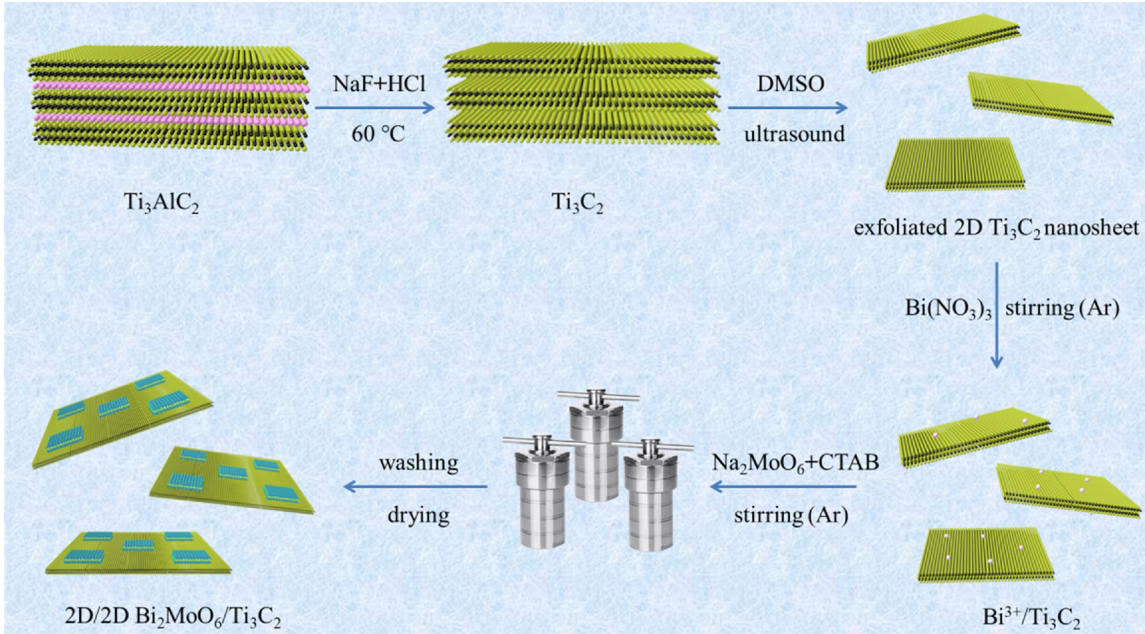

Scheme 1. The diagram of preparation of Ti_3C_2 and Bi_2MoO_6/Ti_3C_2.

2.5. Photoelectrochemical measurements

The photoelectrochemical properties of the as-obtained photocatalysts were tested on electrochemical workstation with standard three-electrode system, which photocatalyst loaded fluorine doped tin oxide conductive glass, platinum sheet, and standard Ag/AgCl electrode were separately employed as working electrode, counter electrode, and reference electrode. In typically measurement process, the three electrodes were submersed in 0.2 M of Na_2SO_4. TPC, OCP, and EIS that employed for assessing photoinduced electron-hole separation and migration were recorded by this standard three-electrode system.

2.6. Photocatalytic performance evaluation

The photocatalytic properties of prepared photocatalysts were examined by photodegradation of tetracycline (TTC). A 300 W xenon lamp (> 420 nm) served as light source. Typically, 30 mg of catalyst was evenly scattered in 100 mL of solution contained 20 mg L^{-1} of TTC. Before exposing to the xenon lamp, the mixture was stirred for 1 h under dark condition to obtain the adsorption saturation state. In photocatalytic experiment, 4 mL of sample was extracted every 15 min, and then filtrated with 0.45 μm microporous membrane to eliminate photocatalyst particle. The concentration of TTC was detected through an UV–vis spectrophotometer (UV-2770, SHIMADZU Corporation, Japan).

2.7. Quantitative determination of $^{\cdot}OH$ and $^{\cdot}O_2^-$

The contents of $^{\cdot}OH$ and $^{\cdot}O_2^-$ radicals generated in reaction process were determined by the terephthalic acid (TPA) probe means and nitroblue tetrazolium (NBT) transformation method, respectively. TPA could react with $^{\cdot}OH$ in a molar ratio of 1:1 to generate 2-hydroxyterephthalic acid, which has strong fluorescence at 425 nm. The fluorescence was recorded on TBS-380 Fluorometer (Turner Biosystems, USA) operating at the excitation wavelength of 310 nm and the emission wavelength of 425 nm. NBT could react with $^{\cdot}O_2^-$ in a molar ratio of 1:4 and thus leading to the loss of absorbance at 260 nm. The generated amount of $^{\cdot}O_2^-$ can be obtained by monitoring the concentration change of NBT on a UV–vis spectrophotometer (UV-2770, SHIMADZU Corporation, Japan). The concentrations of TPA and NBT were 50 mM and 0.01 mM, respectively.

3. Results and discussion

3.1. Characterization

The crystalline feature of Bi_2MoO_6 and Bi_2MoO_6/Ti_3C_2 were detected by XRD. As for pure Bi_2MoO_6, the 2θ value at 28.26°, 32.54°, 46.82°, 55.70° are ascribed to (131), (060), (062), (133) plane of orthorhombic Bi_2MoO_6 phase (Fig. 1a). For Ti_3C_2, the peaks at 19.36°, 26.56°, 36.02°, 41.78°, 60.76° are ascribed to (004), (006), (202), (105), and (110) reflection of Ti_3C_2 [33]. After uniting Ti_3C_2 with Bi_2MoO_6, the all characteristic absorption band attributed to Bi_2MoO_6 are observed in Bi_2MoO_6/Ti_3C_2 Schottky photocatalyst, revealing that the incorporation of Ti_3C_2 makes no difference on crystalline feature of Bi_2MoO_6. However, the diffraction peaks ascribed to Ti_3C_2 cannot be found in the hybrid material, which is because of its low content (1 %). In Bi_2MoO_6 FT-IR spectra, the peaks of 447 and 572 cm^{-1} relate to Bi-O deformation vibration and stretching vibration (Figs. 1b and S1) [34]. The band situated at 725 cm^{-1} is well matched with asymmetric stretching mode of MoO_6 involving vibrations of the equatorial oxygen atoms [35]. The bands at 797 and 843 cm^{-1} are associated with the asymmetric and symmetric stretching mode of MoO_6 involving vibrations of the apical oxygen atoms [36]. In addition, the peak located at 1628 cm^{-1} is geared to O−H stretching and deformation vibrations of absorbed water [37]. After recombining Bi_2MoO_6 with Ti_3C_2, no FT-IR peak attributed to Ti_3C_2 is detected in 2D/2D Bi_2MoO_6/Ti_3C_2 Schottky heterojunction and all peaks belong to Bi_2MoO_6, which is attributed to the low content of Ti_3C_2 (1 %).

TEM result shows that pristine Bi_2MoO_6 displays the 2D ultrathin nanostructure with length and width of 50 − 100 nm (Fig. 2a). In addition, the exfoliated Ti_3C_2 also displays the ultrathin 2D nanosheet (Fig. 2b). After hydrothermal reaction, Bi_2MoO_6 ultrathin nanosheets are attached to the surface of Ti_3C_2 (Fig. 2c). And an obvious boundary between Bi_2MoO_6 and Ti_3C_2 can be observed in high resolution TEM, and the palpable lattice fringes spacing of 0.264 and 0.320 nm are observed, which are in accordance with the (0110) and (131) atomic plane of Ti_3C_2 and Bi_2MoO_6 [31,38] (Fig. 2d), confirming the intimate contact between Ti_3C_2 and Bi_2MoO_6. In AFM image and the corresponding height profile, the height of 1.98 nm is ascribed to the

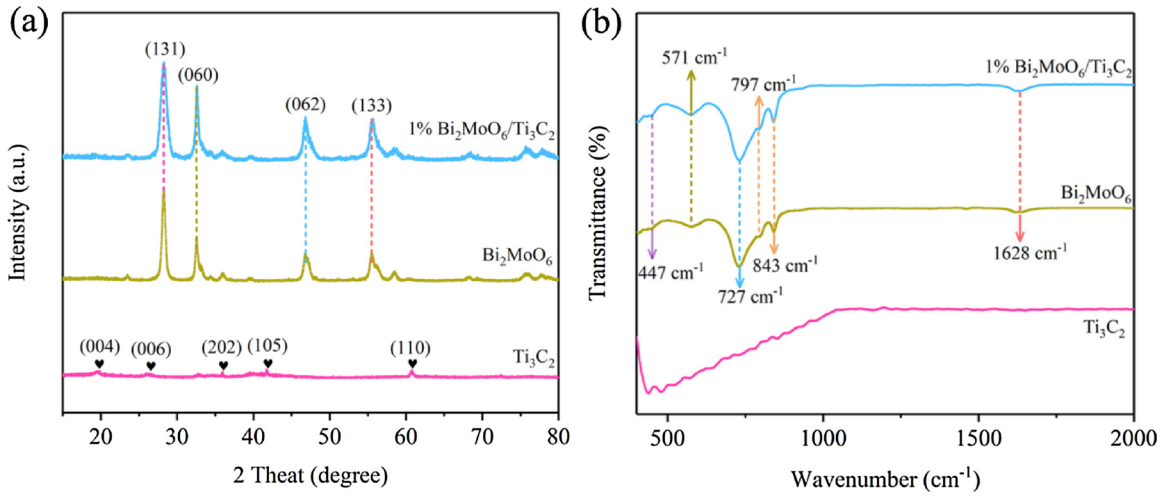

Fig. 1. (a) XRD pattern of Bi_2MoO_6, Ti_3C_2 and 1 % Bi_2MoO_6/Ti_3C_2, (b) FT-IR spectra of Bi_2MoO_6, Ti_3C_2 and 1 % Bi_2MoO_6/Ti_3C_2.

thickness of ultrathin Ti_3C_2 nanosheet, and the height of 1.02 nm and 2.75 nm is in accordance with the monolayer and triple-layers of Bi_2MoO_6, which indicates that Bi_2MoO_6 ultrathin nanosheet has been successfully grown on the surface of Ti_3C_2 nanosheet (Fig. 2e–g). TEM and the corresponding EDS elemental mapping and EDX technology were employed to test the element composition and distribution of Bi_2MoO_6/Ti_3C_2 hybrid material. The result shows that the elements of C, Ti, O, Mo, and Bi have a great distribution in Bi_2MoO_6/Ti_3C_2 (Figs. 2h–m and S2). All results strongly reveal the uniform and intimate coupling between Ti_3C_2 and Bi_2MoO_6 nanosheets, in other words, 2D/2D Bi_2MoO_6/Ti_3C_2 MXene Schottky photocatalyst has been successfully prepared by anaerobically hydrothermal method. Such Schottky heterojunction holds large contact area between cocatalyst and photocatalyst, which may accelerate the migration of photoinduced electron from Bi_2MoO_6 to Ti_3C_2.

The surface chemical composite and chemical environment of synthetized photocatalysts was tested by XPS analysis. As displayed in Fig. 3a, Bi, Mo, and O coexist in Bi_2MoO_6, and Ti, C, O, and F coexist Ti_3C_2. However, only Bi, Mo, O, and C can be found in Bi_2MoO_6/Ti_3C_2, while Ti and F cannot be observed. This is because that the intensity of elements in Ti_3C_2 is relatively weak comparing with elements in Bi_2MoO_6 and the low content of Ti_3C_2 (1 %). In high-resolution picture, two peaks seated at 159.15 and 164.45 eV appertain to Bi $4f_{3/2}$ and Bi $4f_{5/2}$, revealing its trivalent form (Fig. 3b) [39]. Fig. 3c illustrates the high resolution spectrum of Mo 3d, which is compartmentalized into two peaks (235.50 and 232.50 eV), correlating with the Mo $3d_{3/2}$ and Mo $3d_{5/2}$, respectively. And element O is compartmentalized into two peaks (531.30 and 530.25 eV), which are associated with adsorbed H_2O and lattice oxygen (Fig. 3d) [40]. The binding energies at 282.25, 284.80, 286.70, and 289.20 eV in C1s spectrum are correlated with C—Ti, C—C, C—O, and C—F, respectively (Fig. 3e) [41]. While the C—Ti bond in 1 % Bi_2MoO_6/Ti_3C_2 is disappeared. Therefore, the XPS measurement of 1 % Bi_2MoO_6/Ti_3C_2 (prepared by mechanical mixing of Bi_2MoO_6 and Ti_3C_2 for several minutes) was also conducted, the result shows that C—Ti bond retains in C 1s spectra (Fig. S3). This result indicates that the disappearance of C—Ti bond is because that partial C—Ti is disrupted during the preparation process, which is in line with previous studies [26,33,42,43]. Ti 2p can be split into six peaks at 454.90, 456.55, 458.45, 460.85, 462.50, and 465.20 eV, which are in line with Ti(III) $2p_{3/2}$, Ti(II) $2p_{3/2}$, Ti(IV) $2p_{3/2}$, Ti(II) $2p_{1/2}$, Ti(III) $2p_{1/2}$ and Ti(IV) $2p_{1/2}$, respectively (Fig. 3f) [44]. The low valance species of Ti could act as electron donors to activate molecular oxygen owing to its high reduction ability [45]. In high resolution spectrum of F, the binding energies at 688.85 and 685.45 eV are attributed to F—C and F-Ti [27]. Unfortunately, the peaks of Ti and F in Bi_2MoO_6/Ti_3C_2 cannot be accurately differentiated, because they overlap with Bi 4d and Bi 4p, but we can observe that the binding energy of Ti in Bi_2MoO_6/Ti_3C_2 has a negative shift (Figs. S4 and S5). The positive binding energy shift of Bi, Mo, and O and the negative binding energy shift of Ti in Bi_2MoO_6/Ti_3C_2 reveal that electrons are migrated from Bi_2MoO_6 to Ti_3C_2 because the binding energy in XPS has negative correlation with surface electron density, thereby resulting in formation of Schottky junction between Bi_2MoO_6 and Ti_3C_2 interface [46].

The optical property of pristine Bi_2MoO_6 and Bi_2MoO_6/Ti_3C_2 was investigated via UV–vis DRS. The absorption edge of pristine Bi_2MoO_6 locates at approximate 470 nm and the absorption edge of Bi_2MoO_6/Ti_3C_2 2D/2D heterojunction also remains unchanged (Fig. 4a), while the light absorption intensity has a slight enhancement. The appeared phenomenon is because that the existence of Ti_3C_2 nanosheet barely increases the absorption baseline related with the distinct adsorption of carbonaceous materials [47]. The band gap of various materials is acquired through Kubelka-Munk equation [48,49], and the band gap of Bi_2MoO_6 and 1 % Bi_2MoO_6/Ti_3C_2 is 2.77 and 2.76 eV (Fig. 4b). There is no overt difference between absorption edge and band gap of Bi_2MoO_6 and Bi_2MoO_6/Ti_3C_2, indicating photoabsorption is not the primary reason that impacts their photocatalytic performance. Mott-Schottky is regarded as a powerful tool to ascertain the CB potential of photocatalyst. It can be detected from Mott-Schottky plots that Bi_2MoO_6 possesses the positive slope at diverse frequencies (from 1000 to 3000 Hz), revealing the typical n-type feature of Bi_2MoO_6 (Fig. 4c) [50]. In addition, the flat band potential of Bi_2MoO_6 is −0.55 eV from the intercept of the tangent of the Mott-Schottky plots on x-axis (Fig. 4c). In general, the CB potential of n-type semiconductor is close to the flat band potential. Moreover, Ag/AgCl electrode potential is converted into normal hydrogen electrode potential (NHE) based on undermentioned formula:

$$E(NHE)=E(Ag/AgCl)-E^{\theta}+0.059pH \quad (1)$$

Where $E^{\theta}(Ag/AgCl)$ = 0.197 eV [51], thereby the CB potential of Bi_2MoO_6 is -0.42, and the corresponding VB potential is +2.35 eV. In addition, the XPS-VB technology further determines that CB and VB potential of Bi_2MoO_6 is −0.47 and +2.30 eV (Fig. 4d–e), which is in line with the result of Mott-Schottky

For the purpose of exploring the photoinduced charge carrier transfer dynamics, a series of photoelectrochemical methods were conducted, including EIS, OCP, and TPC. As exhibited in Fig. 5a, 1 % Bi_2MoO_6/Ti_3C_2 displays a much smaller arc radiuses of EIS Nyquist curve than pure Bi_2MoO_6, suggesting the smaller photogenerated charge migrate resistance, thereby resulting in high-speed interfacial charge carrier transfer across the contact surface [52]. The surface

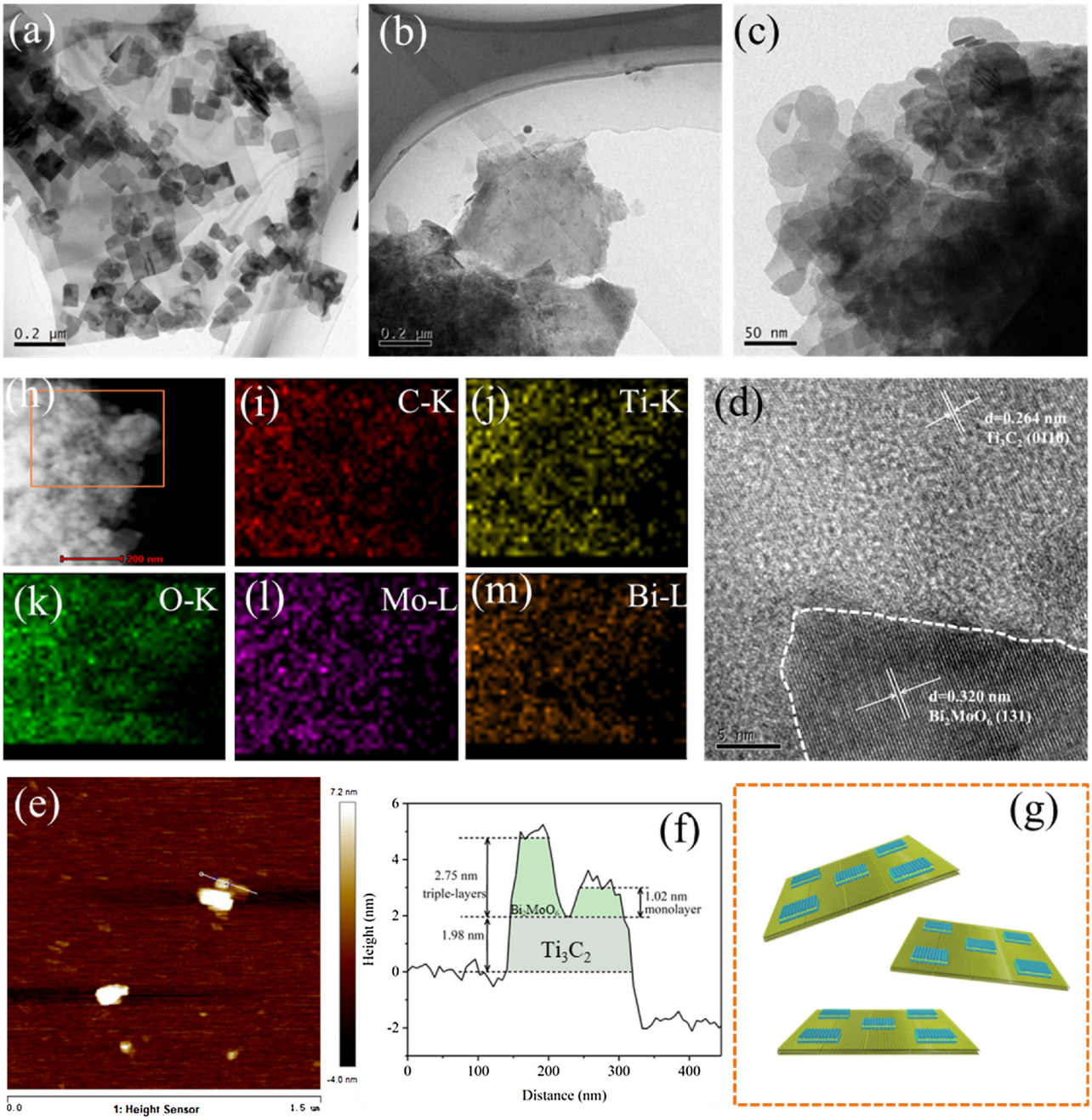

Fig. 2. (a–c) TEM images of pristine Bi_2MoO_6, Ti_3C_2, and 1 % Bi_2MoO_6/Ti_3C_2 MXene Schottky photocatalyst, (d) high resolution TEM of 1 % Bi_2MoO_6/Ti_3C_2, (e–f) AFM image and the corresponding height profiles of 1 % Bi_2MoO_6/Ti_3C_2, (g) the proposed nanostructure of 1 % Bi_2MoO_6/Ti_3C_2, (h–m) TEM image and corresponding EDS elemental mapping of 1 % Bi_2MoO_6/Ti_3C_2.

recombination constant of Bi_2MoO_6 and 1 % Bi_2MoO_6/Ti_3C_2 is investigated by the decay profile of OCP. The average recombination constant is determined by Eq. (2) [53]:

$$\frac{E-E_P}{E_d - E_p}=1-\exp^{-kt} \tag{2}$$

E denotes OCP at any time, E_d denotes OCP stationary value in the dark environment, and E_p denotes photo-stationary OCP value, and k represents the pseudo-first order recombination rate constant (s^{-1}). The OCP transient decay indicates the charge recombination between trapped electrons and adsorbed species on the photocatalyst surface rather than in the lattice bulk, because the slow OCP decay is observed in experiment for several minutes while charge recombination in lattice bulk is very fast (ns–ms domain) [54]. As displayed in Fig. 5b, 1 % Bi_2MoO_6/Ti_3C_2 possesses a much slower transient OCP profile compared to pristine Bi_2MoO_6, indicating that Ti_3C_2 MXene impedes the surface recombination of photogenerated charge carrier. The surface recombination constant of 1 % Bi_2MoO_6/Ti_3C_2 is determined to be 0.0019 s^{-1}, which is 1.63-fold smaller than pure Bi_2MoO_6 (0.0031 s^{-1}), confirming that 1 % Bi_2MoO_6/Ti_3C_2 holds a small surface recombination rate.

TPC measurement indicates that 1 % Bi_2MoO_6/Ti_3C_2 possesses a much larger photocurrent density than pure Bi_2MoO_6 (Fig. 5c–d), revealing its higher photoinduced charge carrier separation efficiency [55]. Meanwhile, the surface charge transfer efficiency (η_t) is studied through the addition of fast electrons scavenger (H_2O_2) into electrolyte [56]. The photocurrent can be defined by the undermentioned Eq. (3):

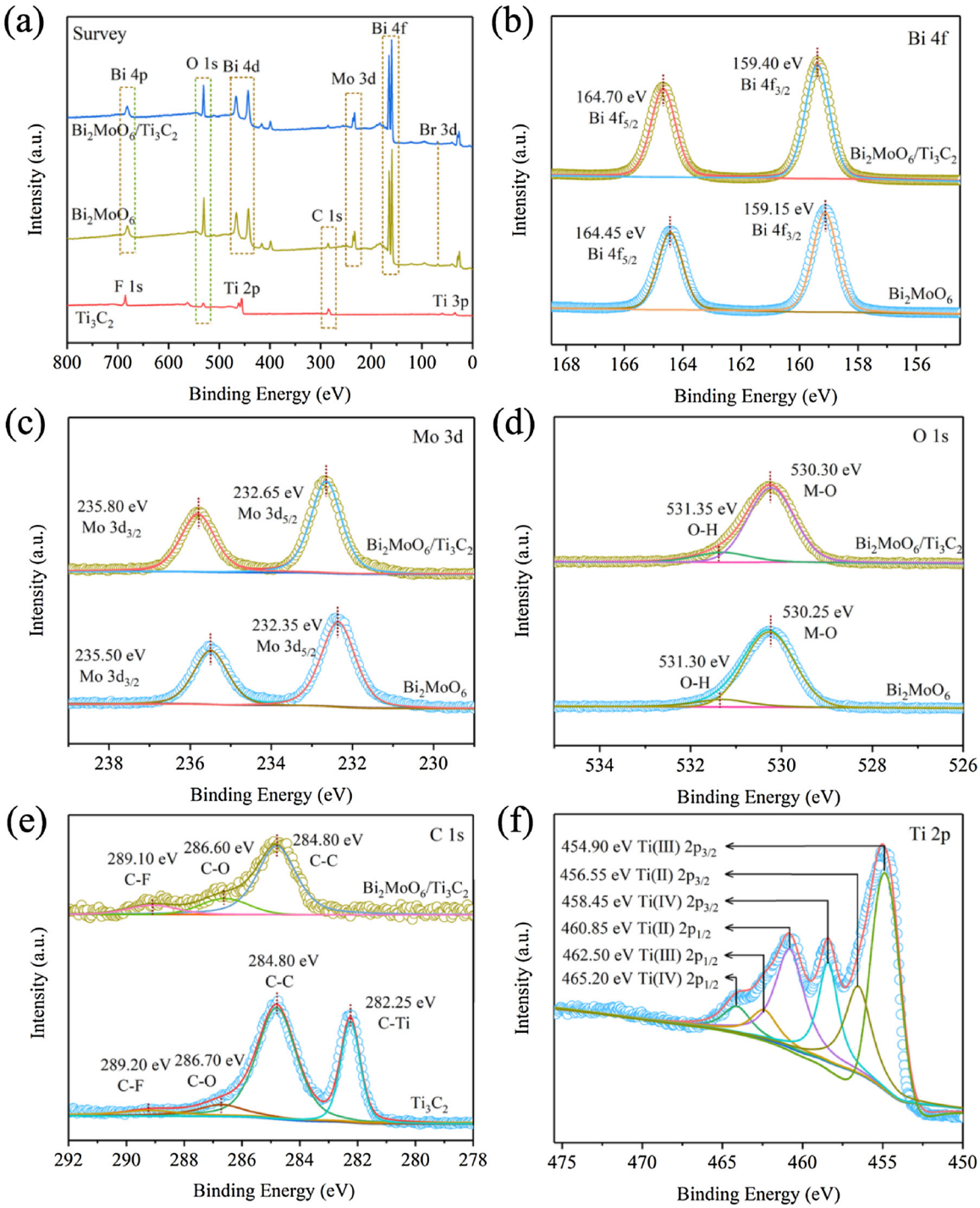

Fig. 3. XPS spectra of Bi_2MoO_6, Ti_3C_2, and 1 % Bi_2MoO_6/Ti_3C_2: (a) survey spectrum; and high resolution of (b) Bi 4f, (c) Mo 3d, (d) O 1s, (e) C 1s, (f) Ti 2p.

$$J_{H_2O} = J_{max}\eta_{abs}\eta_{sep}\eta_{trans} \quad (3)$$

When H_2O_2 is added into electrolyte solution, the surface charge transfer become extremely fast and the η_{trans} approximately reaches 100 %, and then the photogenerated current can be expressed as Eq. (4):

$$J_{H_2O_2} = J_{max}\eta_{abs}\eta_{sep} \quad (4)$$

Here, J_{max}, η_{abs}, η_{sep} do not change in both J_{H_2O} and $J_{H_2O_2}$ system. Consequently, the η_{trans} can be conveyed as following Eq. (5):

$$\eta_{trans} = \frac{J_{H_2O}}{J_{H_2O_2}} \quad (5)$$

As displayed in Fig. 5c–d, the photocurrent of Bi_2MoO_6 raises from 0.019 μA cm^{-2} to 0.103 μA cm^{-2} after adding H_2O_2 into electrolyte solution, while the photogenerated current of Bi_2MoO_6/Ti_3C_2 increases from 0.067 μA cm^{-2} to 0.218 μA cm^{-2}. This phenomenon is attributed to that H_2O_2 is much more easily reduced than that of H_2O. Accordingly, the η_t of Bi_2MoO_6 and Bi_2MoO_6/Ti_3C_2 is calculated to be 18.45 % and 30.73 %, respectively. This result reveals that 2D/2D Bi_2MoO_6/Ti_3C_2 MXene Schottky photocatalyst holds much higher surface charge transfer efficiency than pristine Bi_2MoO_6.

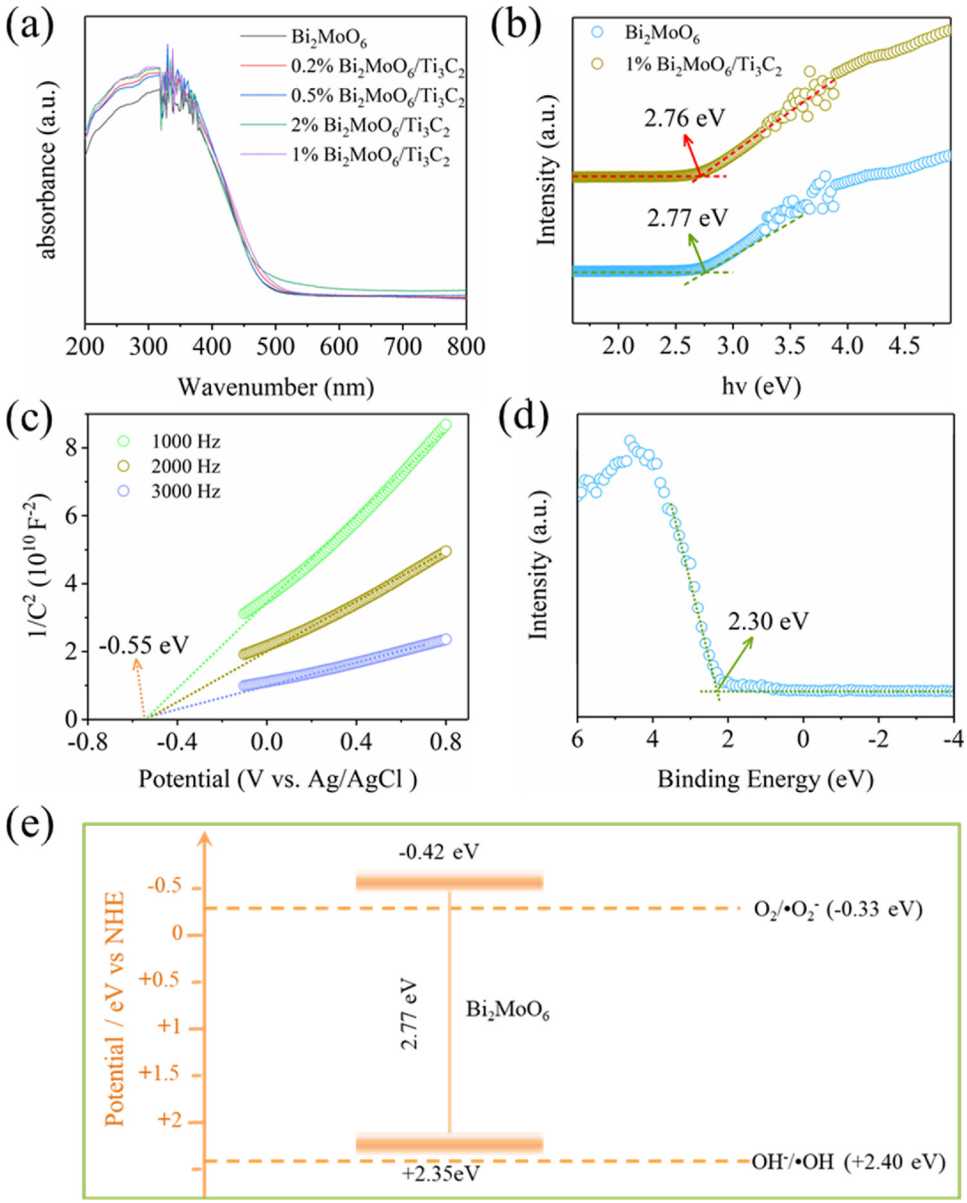

Fig. 4. (a) UV–vis DRS spectra of pristine Bi_2MoO_6 and Bi_2MoO_6/Ti_3C_2 hybrid materials with different content of Ti_3C_2, (b) the band gaps of pristine Bi_2MoO_6 and 1 % Bi_2MoO_6/Ti_3C_2 hybrid materials, (c) the Mott-Schottky curves of pristine Bi_2MoO_6 at different frequencies (from 1000 to 3000 Hz), (d) the XPS-VB spectra of pristine Bi_2MoO_6, (e) Schematic band structures of pristine Bi_2MoO_6 (based on the result of Mott-Schottky).

3.2. Photocatalytic activity assessment

In this study, antibiotic is selected as representative refractory organic contaminant to assess the catalytic performance of Bi_2MoO_6 and Bi_2MoO_6/Ti_3C_2 Schottky photocatalysts owing to its wide employment in iatrology, animal husbandry and agriculture [57,58]. As shown in Fig. 6a, no palpable degradation efficiency is detected without adding photocatalyst into system under visible light irradiation, indicating that pure photolysis exerts no influence on TTC degradation. The catalytic degradation efficiency of pure Bi_2MoO_6 is 57.25 %, while the photodegradation efficiencies of Bi_2MoO_6/Ti_3C_2 hybrid materials with different content of Ti_3C_2 are improved, and the optimal content of Ti_3C_2 is 1 % (mass ratio of Ti_3C_2 to Bi_2MoO_6), about 85.45 % of TTC can be decontaminated within 90 min, indicating that the combination of Ti_3C_2 with Bi_2MoO_6 indeed promotes the photocatalytic property of pure Bi_2MoO_6. In addition, the photodegradation process was further thoroughly understood via pseudo first-order kinetic model. The apparent rate constant (k_{app}) of bare Bi_2MoO_6 for TTC photodegradation is 0.0094 min^{-1}, while the k_{app} for 1 % Bi_2MoO_6/Ti_3C_2 is 0.0214 min^{-1}, which is 2.3 fold higher than pure Bi_2MoO_6 (Fig. 6b), which further confirms that Ti_3C_2 can accelerate photogenerated charge carrier separation and transfer, thereby improving photocatalytic performance.

The practicability and stability are critical factors in the actual wastewater treatment. In this study, four actual wastewaters (river water (RW), lake water (LW), industrial wastewater (IW), medical wastewater (MW)) are selected to assess its practicability. As displayed in Fig. 6c, the photodegradation efficiency is almost no reductive when Bi_2MoO_6/Ti_3C_2 was applied to treat RW and LW. However, the removal efficiency has a slightly reduction when IW and MW was treated. This may be because that many other pollutants coexist in IW and MW to compete with TTC for the limited active species. Nevertheless, the photocatalytic performance for treating these actual wastewaters is still satisfactory. In addition, the photostability of 1 % Bi_2MoO_6/Ti_3C_2 is also tested through cycle experiment. As shown in Fig. 6d, 1 % Bi_2MoO_6/Ti_3C_2 still maintains high photocatalytic performance for TTC

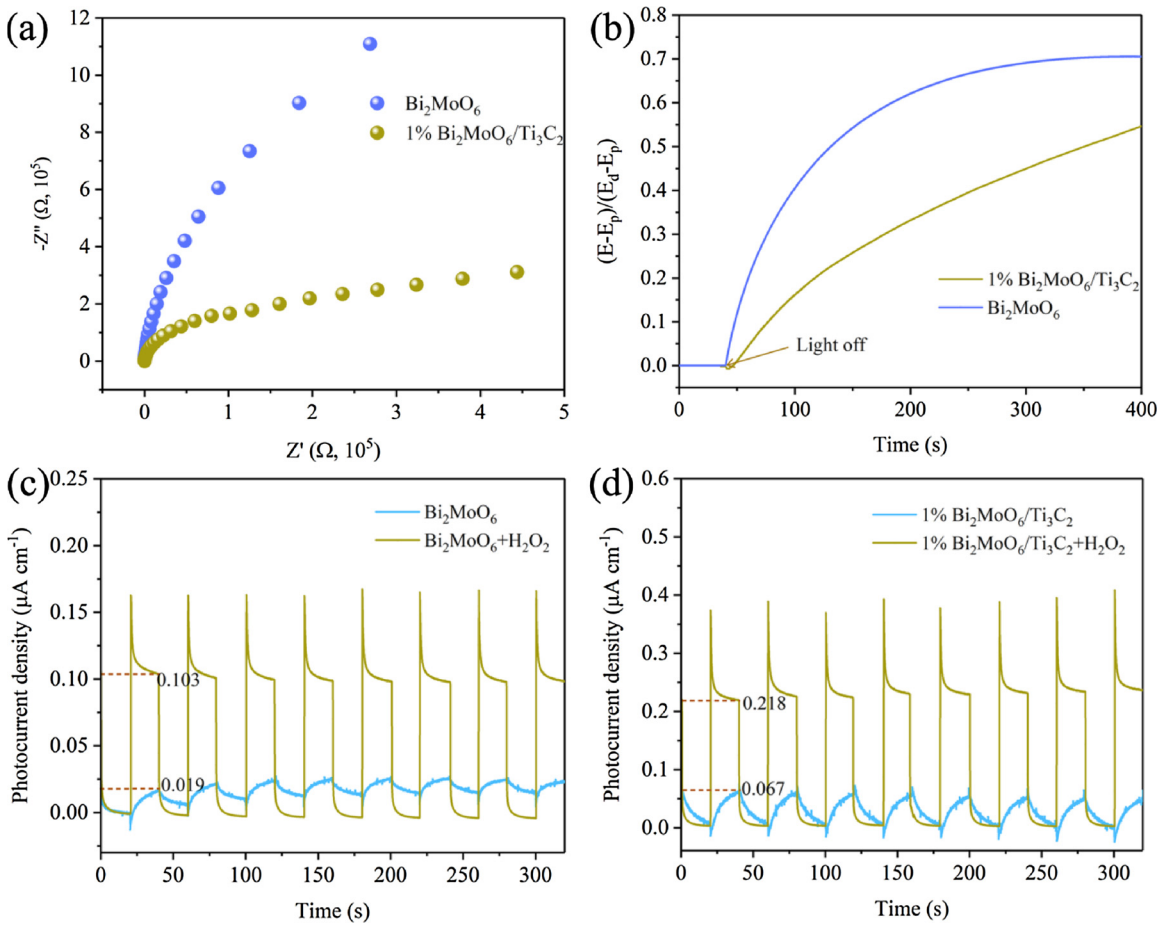

Fig. 5. (a) EIS Nyquist plots of Bi_2MoO_6 and 1 % Bi_2MoO_6/Ti_3C_2, (b) Normalized open-circuit potential (OCP) decay curves after turning off the visible light (n > 420 nm), (c) the photocurrent response of Bi_2MoO_6 without and with adding H_2O_2 into electrolyte, (d) the photocurrent response of 1 % Bi_2MoO_6/Ti_3C_2 without and with adding H_2O_2 into electrolyte.

removal after five successive operations. And XRD pattern of the fresh and used 1 % Bi_2MoO_6/Ti_3C_2 shows that the component and crystalline phase does not change, further confirming the high photostability of 1 % Bi_2MoO_6/Ti_3C_2 (Fig. S6). Consequently, this 2D/2D Schottky photocatalyst is expected to become a rising star material for actual sewage treatment.

3.3. Mechanism exploration

For the sake of exploring the photocatalysis mechanism of Bi_2MoO_6/Ti_3C_2, the generated ROS in catalytic process were investigated. In this work, ethanol (ETA), tert-Butanol (TB), 4-Hydroxy-2,2,6,6-tetramethylpiperidine 1-Oxyl Free Radical (TEMPOL), and L-tryptophan (LTP) are utilized as scavengers of h^+, $^{\cdot}OH$, $^{\cdot}O_2^-$, and $^1O_2$, respectively. As displayed in Fig. 7, the photocatalytic performance is restrained when adding TEMPOL, ETA, TB, and LTP into catalytic process, only 46.79 %, 52.73 %, 57.09 %, and 63.92 % of TTC can be decontaminated, which indicates that $^{\cdot}O_2^-$, h^+, $^{\cdot}OH$, and $^1O_2$ are major ROS participated in catalytic reaction. In order to further identify the generation of aforementioned ROS, ESR technology is employed. The result shows that the signal attributed DMPO-$^{\cdot}O_2^-$ appears when 1 % Bi_2MoO_6/Ti_3C_2 exposes to visible light illumination, while no signal can be found in dark, suggesting $^{\cdot}O_2^-$ indeed generates in photocatalytic system. Meanwhile, the ESR signals of DMPO-$^{\cdot}O_2^-$ and TEMP-$^1O_2$ are also detected after 1 % Bi_2MoO_6/Ti_3C_2 suffering from light illumination, confirming the formation of $^{\cdot}OH$ and $^1O_2$.

In addition, NBT transformation method was employed to quantitative determine the yield of $^{\cdot}O_2^-$ [59]. NBT could react with $^{\cdot}O_2^-$ in a molar ratio of 1:4 and thus lead to the loss of absorbance at 260 nm. The generated amount of $^{\cdot}O_2^-$ can be obtained by monitoring the concentration change of NBT. As displayed in Fig. S7-8, the density of the absorbance at 260 nm of NBT constantly reduces with extension of time after catalytic reaction by 1 % Bi_2MoO_6/Ti_3C_2, while only very few loss of absorbance is detected by Bi_2MoO_6. From Fig. 8a, about 4.07 % and 25.81 % of NBT react with $^{\cdot}O_2^-$ in Bi_2MoO_6 and 1 % Bi_2MoO_6/Ti_3C_2 system, the K_{app} of 1 % Bi_2MoO_6/Ti_3C_2 is much higher than pure Bi_2MoO_6 (Fig. S9), and the corresponding $^{\cdot}O_2^-$ production by Bi_2MoO_6 and 1 % Bi_2MoO_6/Ti_3C_2 are 43.556 μmol L^{-1} g^{-1} and 243.556 μmol L^{-1} g^{-1} (5.56 times) (Fig. 8b). In addition, the production of $^{\cdot}OH$ is also quantitatively determined through TPA probe means [11]. TPA could react with $^{\cdot}OH$ in a molar ratio of 1:1 to generate 2-hydroxyterephthalic acid, which has strong fluorescence at about 425 nm. As displayed in Fig. S10, no characteristic absorption band of 2-hydroxyterephthalic acid is detected after adsorption for 30 min, suggesting adsorption cannot generate $^{\cdot}OH$. However, after visible light irradiation, the characteristic peaks appear and the intensity increase with prolonging lighting time (Figs. S11 and S12). Therefore, the production rate of $^{\cdot}OH$ concentration over Bi_2MoO_6 is determined to be 1.801 μmol L^{-1} g^{-1}, while $^{\cdot}OH$ production rate of 1 % Bi_2MoO_6/Ti_3C_2 can reach 6.908 μmol L^{-1} g^{-1} (3.83 times) (Fig. 8c–d). Nevertheless, the yield of $^{\cdot}OH$ is much lower than $^{\cdot}O_2^-$. More importantly, the VB potential is more negative than oxidation potential of OH-/$^{\cdot}OH$ (+2.40 eV), thereby $^{\cdot}OH$ is unable to generate by hole oxidation. Consequently, the generated $^{\cdot}OH$ is originated from the $^{\cdot}O_2^-$ conversion [60]. In addition, the detected $^1O_2$ is also generated by $^{\cdot}O_2^-$ conversion [61]. Based on aforementioned results, Bi_2MoO_6/Ti_3C_2 2D/2D MXene Schottky photocatalyst is more

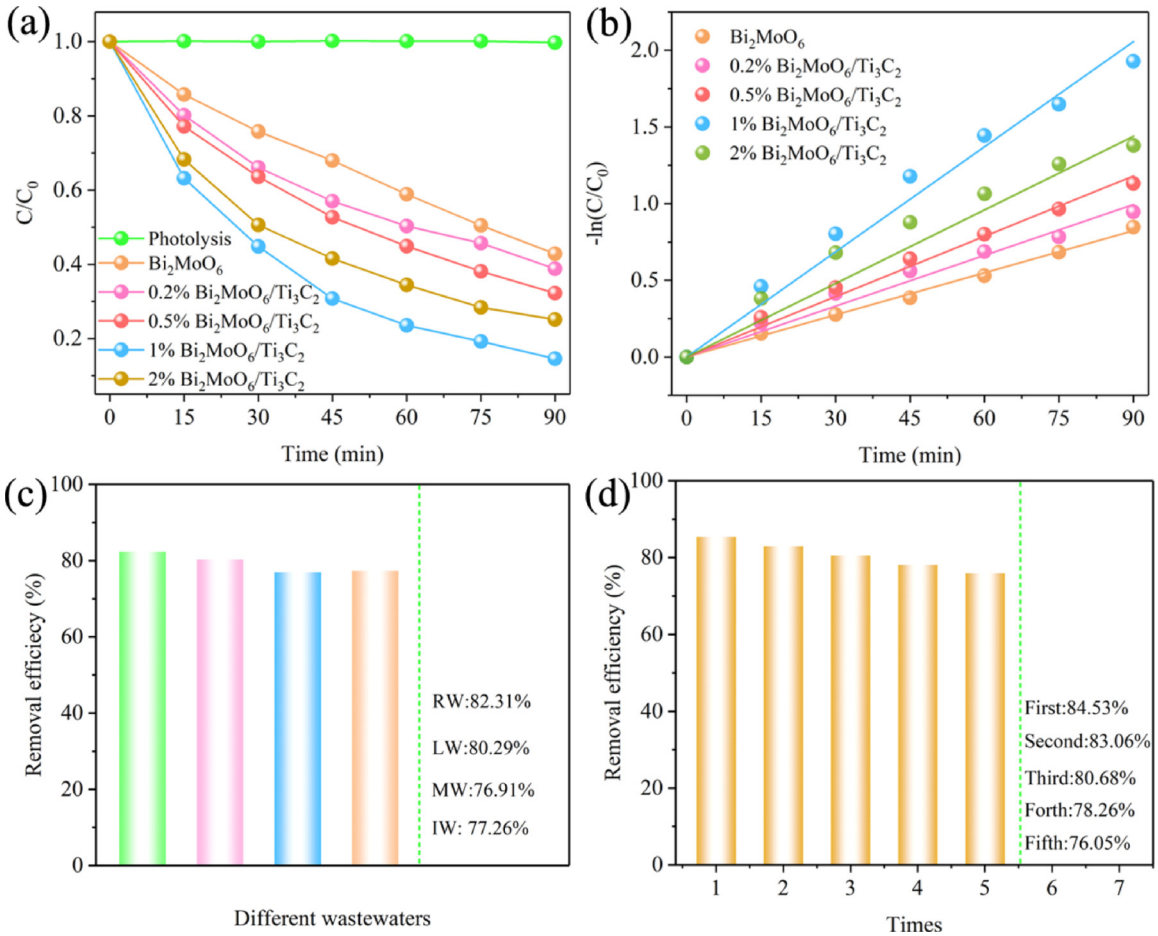

Fig. 6. (a) Photocatalytic degradation of TTC by pure Bi_2MoO_6 and Bi_2MoO_6/Ti_3C_2 Schottky photocatalysts, (b) and the corresponding -ln(C/C_0) versus time curves, (c) The photoctalytic performance of 1 % Bi_2MoO_6/Ti_3C_2 for different wastewaters treatment, (b) the five successive operations for TTC removal by 1 % Bi_2MoO_6/Ti_3C_2.

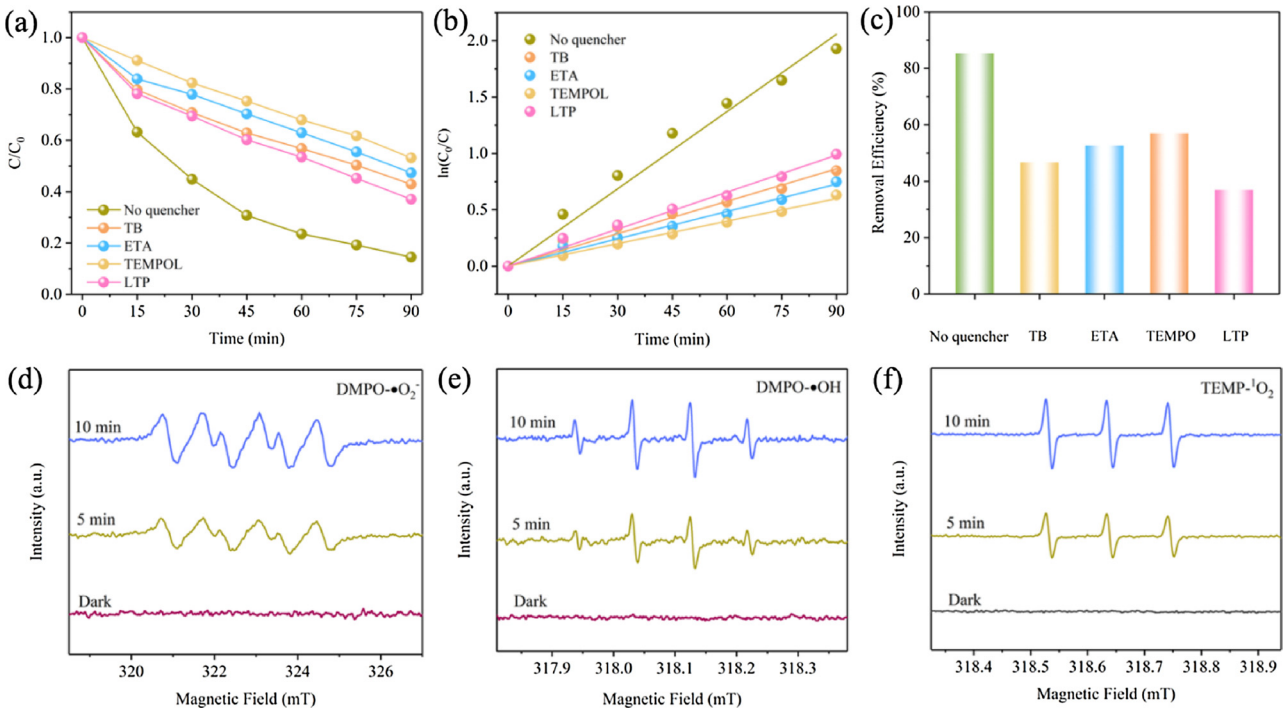

Fig. 7. (a–c) Effect of different scavengers on the photodegradation efficiency of 1 % Bi_2MoO_6/Ti_3C_2, (d–f) and corresponding ESR spectra for DMPO-$^{\cdot}O_2^{-}$, DMPO-$^{\cdot}$OH, and TEMP-$^1O_2$.

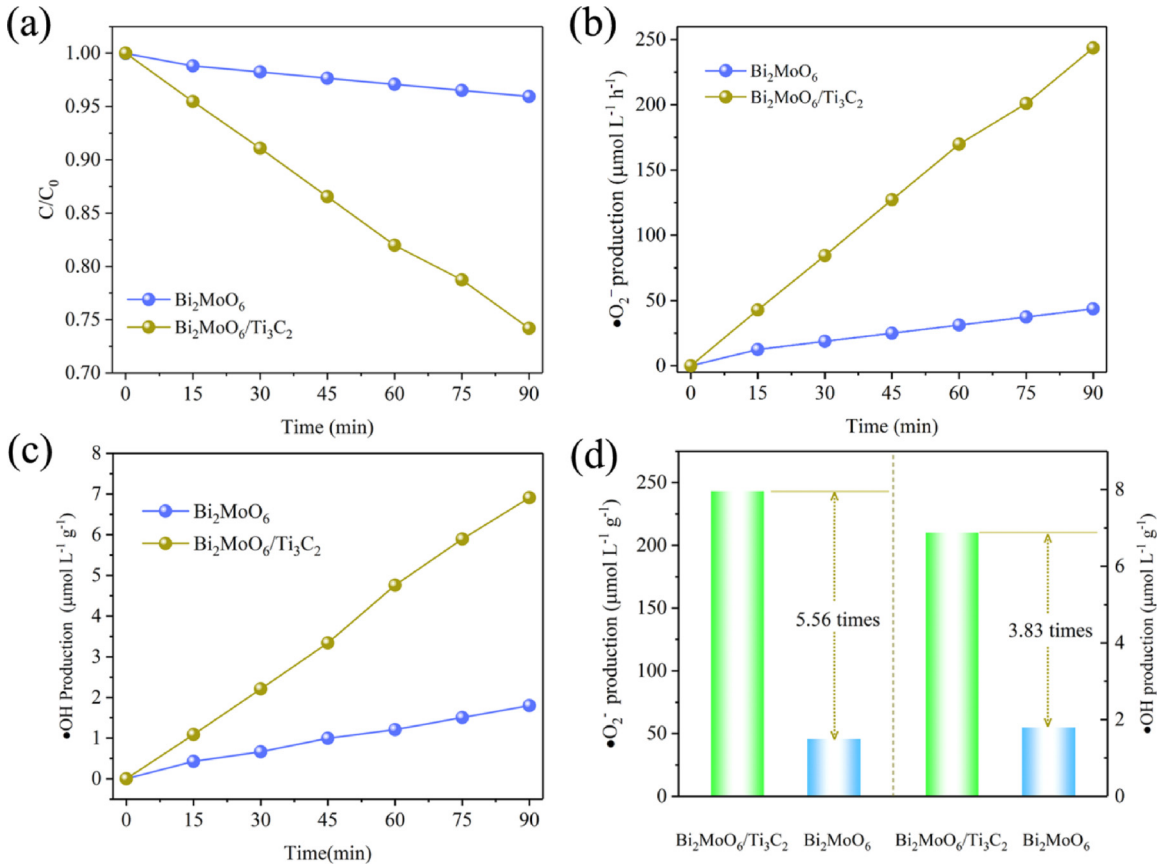

Fig. 8. (a) the photodegradation curves of NBT by Bi_2MoO_6 and 1 % Bi_2MoO_6/Ti_3C_2, (b) and the corresponding $^{\cdot}O_2^{-}$ production, (c) the $^{\cdot}OH$ production rate of Bi_2MoO_6 and 1 % Bi_2MoO_6/Ti_3C_2, (d) the comparison of reactive oxygen species production between Bi_2MoO_6 and 1 % Bi_2MoO_6/Ti_3C_2.

propitious to activate molecular oxygen to generate $^{\cdot}O_2^{-}$, and meanwhile convert to other ROS.

In the light of foregoing results, the potential catalytic mechanism of Bi_2MoO_6/Ti_3C_2 for MOA is put forward and exhibited in Scheme 2. Under visible light irradiation, Bi_2MoO_6 is stimulated and produced electron and hole, the electron first flows to CB of Bi_2MoO_6 (Eq. (7)), and then conquers Schottky barrier to quickly jump to Ti_3C_2 through built-in electric field (Eq. (8)). Previous study has reported that the introduction of Ti_3C_2 was favorable for O_2 adsorption because unsaturated Ti 3d orbitals of Ti_3C_2 can absorb dissolved O_2 molecules through the charge donating defect effect and quasi-alloying effect [62]. Therefore, the migrated photogenerated electron on Ti_3C_2

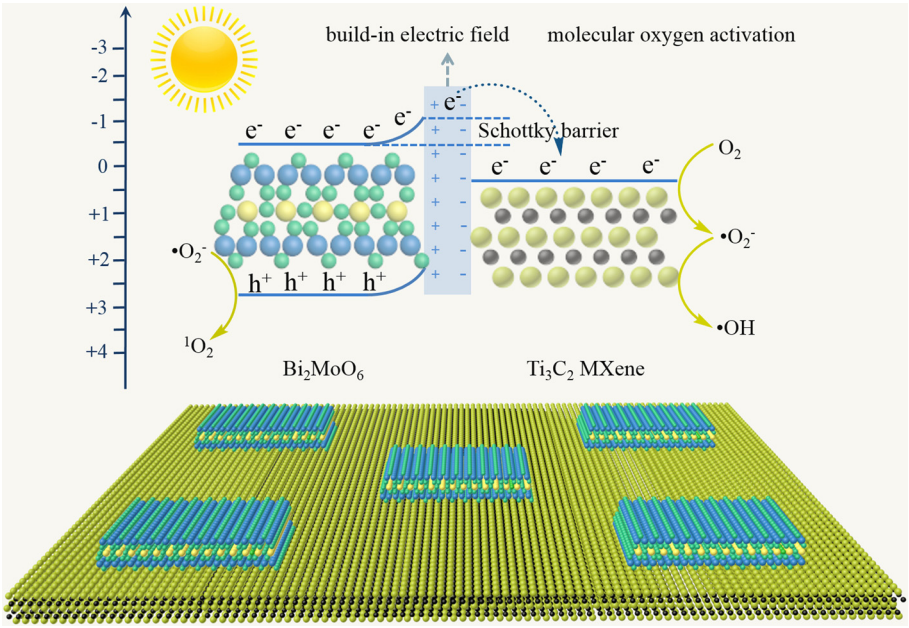

Scheme 2. The possible mechanism for visible light driven molecular oxygen activation.

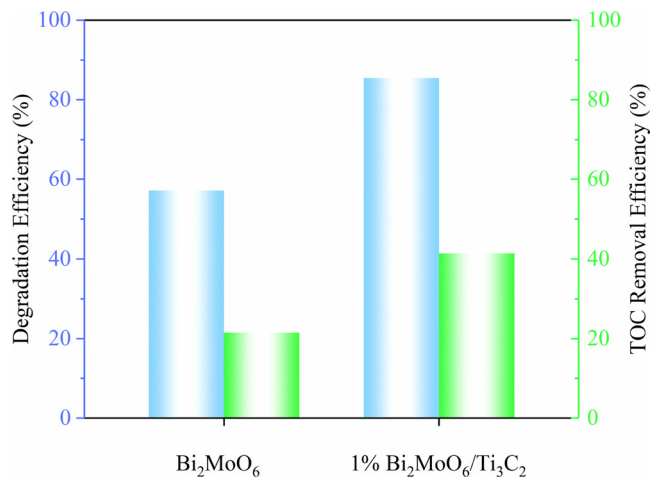

Fig. 9. The photodegradation efficiency and TOC removal efficiency of TTC by Bi_2MoO_6 and 1 % Bi_2MoO_6/Ti_3C_2.

nanosheet can activate absorbed molecular oxygen to generate $^{\cdot}O_2^-$ (Eq. (9)). However, as a result of the more negative VB of Bi_2MoO_6 (2.35 eV < 2.40 eV), $^{\cdot}OH$ cannot be generated through H_2O oxidation by photoinduced h^+ [63]. However, $^{\cdot}OH$ is detected in this system. Therefore, the detected $^{\cdot}OH$ by capture experiment, ESR, and TPA probe means is originated from the $^{\cdot}O_2^-$ translation (Eqs. (10) and (11)) [60]. In addition, capture experiment and ESR also confirm the generation of $^1O_2$ in this system, thus the other part of $^{\cdot}O_2^-$ will react with photoinduced hole to form $^1O_2$ (Eq. (12)) [61]. Thus, in this study, the molecular oxygen is first activated to generate $^{\cdot}O_2^-$, and then converted to other ROS under the action of electrons and holes. The all generated ROS (including $^{\cdot}O_2^-$, $^{\cdot}OH$, and $^1O_2$) by MOA can participate in important catalytic process (pollutant decontamination) owing to their strong oxidation capacity. Meanwhile, the remnant photogenerated hole in CB of Bi_2MoO_6 can also take part in catalytic reaction (pollutant decontamination) (Eq. (13)).

$$Bi_2MoO_6 + hv \rightarrow Bi_2MoO_6(e^-) + Bi_2MoO_6(h^+) \quad (7)$$

$$Bi_2MoO_6(e^-) \rightarrow Ti_3C_2(e^-) \quad (8)$$

$$e^- + O_2 \rightarrow \cdot O_2^- \quad (9)$$

$$\cdot O_2^- + H^+ + e^- \rightarrow H_2O_2 \quad (10)$$

$$H_2O_2 + e^- \rightarrow \cdot OH + OH^- \quad (11)$$

$$\cdot O_2^- + h^+ \rightarrow {}^1O_2 \quad (12)$$

$$\cdot O_2^- + \cdot OH + {}^1O_2 + h^+ + \text{pollutants} \rightarrow \text{production} \quad (13)$$

3.4. Exploration of intermediates and degradation pathways

The mineralization efficiency was measured through total organic carbon [64]. The mineralization efficiency of pristine Bi_2MoO_6 is 21.36 %, while the mineralization efficiency of 1 % Bi_2MoO_6/Ti_3C_2 can reach 41.15 %, which is approximate 1.93 times higher than pristine Bi_2MoO_6, further revealing its excellent photocatalytic performance (Fig. 9). However, it can be found that mineralization rate is lower than photocatalytic removal rate, which reveals that the TTC is transformed into some intermediate products. Therefore, the liquid chromatography-triple quadrupole tandem mass spectrometry (LCMS/MS) was employed to detect these intermediate products and explore the photodegradation pathways. As displayed in Scheme 3, six intermediate products are detected and thus two photodegradation pathways are

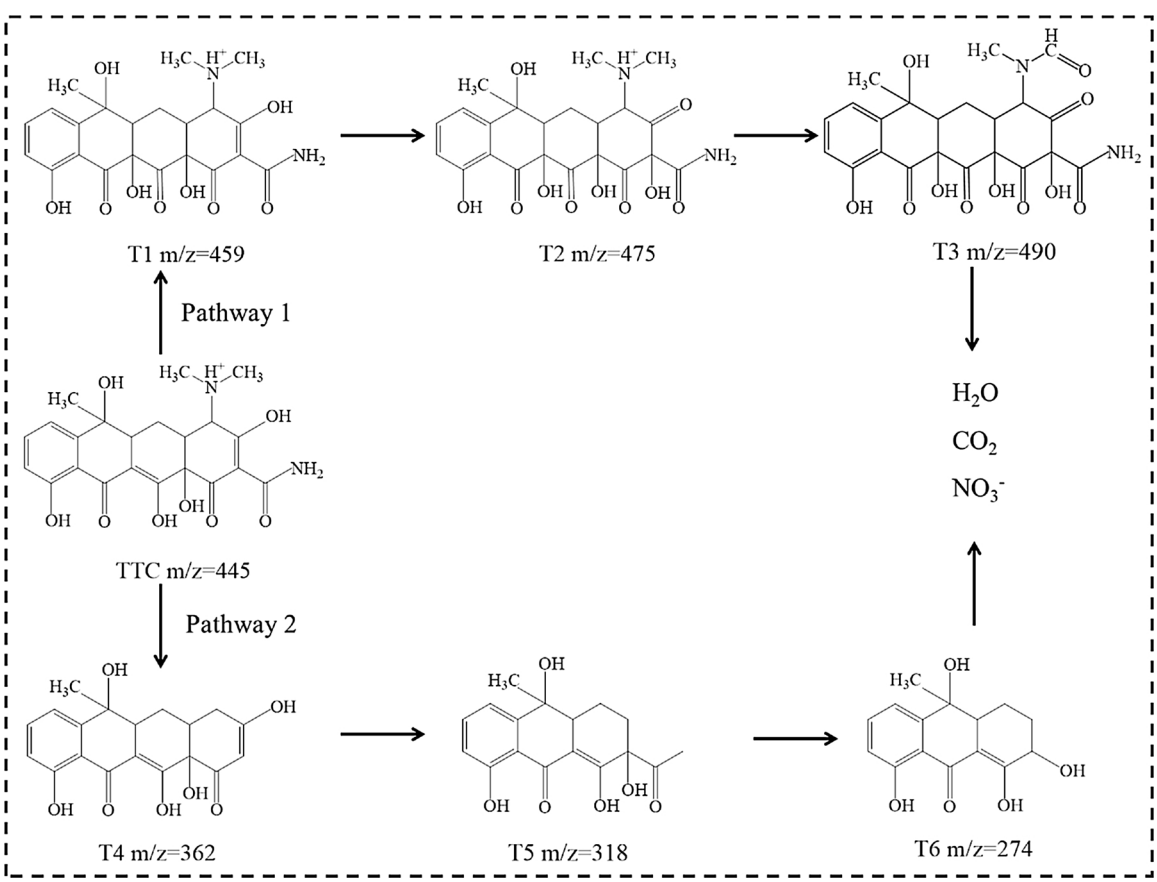

Scheme 3. The proposed photodegradation pathways of TTC by 1 % Bi_2MoO_6/Ti_3C_2.

proposed. As for pathway 1, the intermediate of T1 is produced by the hydroxylation process of original TTC. The product with m/z of 475 (T2) is generated by the $^{\cdot}OH$ attack of generated T1, and T2 is further assaulted by $^{\cdot}OH$ to produce T3 with m/z of 490 [65]. In the term of pathway 2, the intermediate of T4 is generated by undergoing several processes including dehydration of original TTC, the demethylation of the dimethylamino group, and the detachment of the carbinol and acylamino group. The intermediate T5 is originated from the opening of the carboatomic ring in T4, and the decarboxylation of T5 leads to the generation of T6 [66]. Ultimately, the above-produced intermediate products are mineralized into NO_3^-, CO_2, and H_2O.

4. Conclusion

In summary, a novel 2D/2D Bi_2MoO_6/Ti_3C_2 MXene Schottky heterojunction is successfully prepared through facile CTAB-assisted anaerobically hydrothermal method. The as-obtained hybrid material displays excellent photocatalytic performance for MOA compared to pristine Bi_2MoO_6. The enhanced photocatalytic performance is associated with some aspects. On the one hand, the large contact area formed between 2D/2D Schottky heterojunction accelerates the separation and migration of photoexcited electron-hole pairs. On the other hand, the high redox activity of surface Ti sites promotes multi-electron reduction reaction to realize high MOA performance. In brief, this work not only offers a new tactics to design 2D/2D high-performance photocatalytic system, but also gives a deep understanding of MOA on surface structures in photocatalytic reactions.

CRediT author statement

Cui Lai, Guangming Zeng, Danlian Huang conceived and designed the experiments. Bisheng Li, Shiyu Liu, and Mingming Zhang prepared the photocatalysts. Lei Qin and Mingzhu Zhou performed the photocatalytic experiment. Xigui Liu, Zhongwu Li, and Ning An conducted and analyzed the various characterizations; Bisheng Li and Fuhang Xu wrote the manuscript. Huan Yi, Yujin Zhang, and Liang Chen revised the manuscript.

Declaration of Competing Interest

None.

Acknowledgements

This study was financially supported by the Program for the National Natural Science Foundation of China (51779090, 51879101, 51579098, 51709101, 51521006, 51809090, 51909084), the National Program for Support of Top–Notch Young Professionals of China (2014), the Program for Changjiang Scholars and Innovative Research Team in University (IRT-13R17), and Hunan Provincial Science and Technology Plan Project (2018SK20410, 2017SK2243, 2016RS3026), and the Fundamental Research Funds for the Central Universities (531119200086, 531118010114, 531107050978, 541109060031).

Appendix A. Supplementary data

Supplementary material related to this article can be found, in the online version, at doi:https://doi.org/10.1016/j.apcatb.2020.118650.

References

[1] H. Huang, S. Tu, C. Zeng, T. Zhang, A.H. Reshak, Y. Zhang, Angew. Chem. Int. Ed. 56 (2017) 11860–11864.
[2] H. Wang, S. Jiang, S. Chen, D. Li, X. Zhang, W. Shao, X. Sun, J. Xie, Z. Zhao, Q. Zhang, Y. Tian, Y. Xie, Adv. Mater. 28 (2016) 6940–6945.
[3] L. Qin, D. Huang, P. Xu, G. Zeng, C. Lai, Y. Fu, H. Yi, B. Li, C. Zhang, M. Cheng, C. Zhou, X. Wen, J. Colloid Interfaces Sci. 534 (2019) 357–369.
[4] C. Liang, H. Guo, L. Zhang, M. Ruan, C.-G. Niu, H.-P. Feng, X.-J. Wen, N. Tang, H.-Y. Liu, G.-M. Zeng, Chem. Eng. J. 372 (2019) 12–25.
[5] J.M. Anglada, M. Martins-Costa, J.S. Francisco, M.F. Ruiz-Lopez, Acc. Chem. Res. 48 (2015) 575–583.
[6] R. Long, K. Mao, X. Ye, W. Yan, Y. Huang, J. Wang, Y. Fu, X. Wang, X. Wu, Y. Xie, Y. Xiong, J. Am. Chem. Soc. 135 (2013) 3200–3207.
[7] K. Qian, L. Du, X. Zhu, S. Liang, S. Chen, H. Kobayashi, X. Yan, M. Xu, Y. Dai, R. Li, J. Mater. Chem. A 7 (2019) 14592–14601.
[8] H. Wang, X. Sun, D. Li, X. Zhang, S. Chen, W. Shao, Y. Tian, Y. Xie, J. Am. Chem. Soc. 139 (2017) 2468–2473.
[9] M.A. Henderson, I. Lyubinetsky, Chem. Rev. 113 (2013) 4428–4455.
[10] J. Di, C. Zhu, M. Ji, M. Duan, R. Long, C. Yan, K. Gu, J. Xiong, Y. She, J. Xia, H. Li, Z. Liu, Angew. Chem. Int. Ed. 130 (2018) 15063–15067.
[11] S. Wang, X. Ding, X. Zhang, H. Pang, X. Hai, G. Zhan, W. Zhou, H. Song, L. Zhang, H. Chen, J. Ye, Adv. Funct. Mater. 27 (2017) 1703923.
[12] K. Jing, J. Xiong, N. Qin, Y. Song, L. Li, Y. Yu, S. Liang, L. Wu, Chem. Commun. 53 (2017) 8604–8607.
[13] T.S. Dörr, L. Deilmann, G. Haselmann, A. Cherevan, P. Zhang, P. Blaha, P.W. de Oliveira, T. Kraus, D. Eder, Adv. Energy Mater. 8 (2018) 1802566.
[14] H. Yu, J. Li, Y. Zhang, S. Yang, K. Han, F. Dong, T. Ma, H. Huang, Angew. Chem. Int. Ed. 58 (2019) 3880–3884.
[15] B. Li, C. Lai, G. Zeng, L. Qin, H. Yi, D. Huang, C. Zhou, X. Liu, M. Cheng, P. Xu, C. Zhang, F. Huang, S. Liu, ACS Appl. Mater. Interfaces 10 (2018) 18824–18836.
[16] C. Zhou, Z. Zeng, G. Zeng, D. Huang, R. Xiao, M. Cheng, C. Zhang, W. Xiong, C. Lai, Y. Yang, W. Wang, H. Yi, B. Li, J. Hazard. Mater. 380 (2019) 120815.
[17] T. Su, Q. Shao, Z. Qin, Z. Guo, Z. Wu, ACS Catal. 8 (2018) 2253–2276.
[18] B. Li, C. Lai, L. Qin, C. Chu, M. Zhang, S. Liu, X. Liu, H. Yi, J. He, L. Li, M. Li, L. Chen, J. Colloid Interfaces Sci. 560 (2020) 701–713.
[19] W. Gu, F. Lu, C. Wang, S. Kuga, L. Wu, Y. Huang, M. Wu, ACS Appl. Mater. Interfaces 9 (2017) 28674–28684.
[20] B. Mendoza-Sanchez, Y. Gogotsi, Adv. Mater. 28 (2016) 6104–6135.
[21] B. Ahmed, D.H. Anjum, Y. Gogotsi, H.N. Alshareef, Nano Energy 34 (2017) 249–256.
[22] F. Wang, C. Yang, M. Duan, Y. Tang, J. Zhu, Biosens. Bioelectron. 74 (2015) 1022–1028.
[23] M. Naguib, V.N. Mochalin, M.W. Barsoum, Y. Gogotsi, Adv. Mater. 26 (2014) 992–1005.
[24] Z. Ai, Y. Shao, B. Chang, B. Huang, Y. Wu, X. Hao, Appl. Catal. B: Environ. 242 (2019) 202–208.
[25] M. Ghidiu, M.R. Lukatskaya, M.Q. Zhao, Y. Gogotsi, M.W. Barsoum, Nature 516 (2014) 78–81.
[26] T. Cai, L. Wang, Y. Liu, S. Zhang, W. Dong, H. Chen, X. Yi, J. Yuan, X. Xia, C. Liu, S. Luo, Appl. Catal. B: Environ. 239 (2018) 545–554.
[27] J. Ran, G. Gao, F.T. Li, T.Y. Ma, A. Du, S.Z. Qiao, Nat. Commun. 8 (2017) 13907.
[28] H. Wang, Y. Sun, Y. Wu, W. Tu, S. Wu, X. Yuan, G. Zeng, Z.J. Xu, S. Li, J.W. Chew, Appl. Catal. B: Environ. 245 (2019) 290–301.
[29] X. Xie, N. Zhang, Z.-R. Tang, M. Anpo, Y.-J. Xu, Appl. Catal. B: Environ. 237 (2018) 43–49.
[30] L. Pei, T. Li, Y. Yuan, T. Yang, J. Zhong, Z. Ji, S. Yan, Z. Zou, Chem. Commun. 55 (2019) 11754–11757.
[31] O. Mashtalir, M. Naguib, V.N. Mochalin, Y. Dall'Agnese, M. Heon, M.W. Barsoum, Y. Gogotsi, Nat. Commun. 4 (2013) 1716.
[32] F. Liu, A. Zhou, J. Chen, J. Jia, W. Zhou, L. Wang, Q. Hu, Appl. Surf. Sci. 416 (2017) 781–789.
[33] Y. Liu, H. Zeng, Y. Chai, R. Yuan, H. Liu, Chem. Commun. 55 (2019) 13729–13732.
[34] L. Zhang, T. Xu, X. Zhao, Y. Zhu, Appl. Catal. B: Environ. 98 (2010) 138–146.
[35] J. Di, J. Xia, M. Ji, H. Li, H. Xu, H. Li, R. Chen, Nanoscale 7 (2015) 11433–11443.
[36] H. Li, J. Liu, W. Hou, N. Du, R. Zhang, X. Tao, Appl. Catal. B: Environ. 160–161 (2014) 89–97.
[37] D. Ma, J. Wu, M. Gao, Y. Xin, C. Chai, Chem. Eng. J. 316 (2017) 461–470.
[38] T. Hu, Y. Yang, K. Dai, J. Zhang, C. Liang, Appl. Surf. Sci. 456 (2018) 473–481.
[39] H. Yi, M. Yan, D. Huang, G. Zeng, C. Lai, M. Li, X. Huo, L. Qin, S. Liu, X. Liu, B. Li, H. Wang, M. Shen, Y. Fu, X. Guo, Appl. Catal. B: Environ. 250 (2019) 52–62.
[40] M. Zhang, C. Lai, B. Li, D. Huang, G. Zeng, P. Xu, L. Qin, S. Liu, X. Liu, H. Yi, M. Li, C. Chu, Z. Chen, J. Catal. 369 (2019) 469–481.
[41] S. Cao, B. Shen, T. Tong, J. Fu, J. Yu, Adv. Funct. Mater. 28 (2018) 1800136.
[42] N. Li, Y. Jiang, C. Zhou, Y. Xiao, B. Meng, Z. Wang, D. Huang, C. Xing, Z. Peng, ACS Appl. Mater. Interfaces 11 (2019) 38116–38125.
[43] H. Huang, Y. Song, N. Li, D. Chen, Q. Xu, H. Li, J. He, J. Lu, Appl. Catal. B: Environ. 51 (2019) 154–161.
[44] Z. Zhang, H. Li, G. Zou, C. Fernandez, B. Liu, Q. Zhang, J. Hu, Q. Peng, ACS Sustain. Chem. Eng. 4 (2016) 6763–6771.
[45] C. Li, G. Chen, J. Sun, H. Dong, Y. Wang, C. Lv, Appl. Catal. B: Environ. 160–161 (2014) 383–389.
[46] S. Wang, B.Y. Guan, X. Wang, X.W.D. Lou, J. Am. Chem. Soc. 140 (2018) 15145–15148.
[47] Z. Liu, Y. Song, Q. Wang, Y. Jia, X. Tan, X. Du, S. Gao, J. Colloid Interface Sci. 556 (2019) 92–101.
[48] B. Li, C. Lai, P. Xu, G. Zeng, D. Huang, L. Qin, H. Yi, M. Cheng, L. Wang, F. Huang, S. Liu, M. Zhang, J. Clean. Prod. 225 (2019) 898–912.
[49] M. Zhang, C. Lai, B. Li, D. Huang, S. Liu, L. Qin, H. Yi, Y. Fu, F. Xu, M. Li, L. Li, J. Colloid Interface Sci. 556 (2019) 557–567.
[50] X. Sun, X. Luo, X. Zhang, J. Xie, S. Jin, H. Wang, X. Zheng, X. Wu, Y. Xie, J. Am. Chem. Soc. 141 (2019) 3797–3801.
[51] W. Zhou, J. Jia, J. Lu, L. Yang, D. Hou, G. Li, S. Chen, Nano Energy 28 (2016) 29–43.

[52] C. Lai, S. Liu, C. Zhang, G. Zeng, D. Huang, L. Qin, X. Liu, H. Yi, R. Wang, F. Huang, B. Li, T. Hu, ACS Sens. 3 (2018) 2566–2573.
[53] Z. Jiang, H. Sun, T. Wang, B. Wang, W. Wei, H. Li, S. Yuan, T. An, H. Zhao, J. Yu, P.K. Wong, Energy Environ. Sci. 11 (2018) 2382–2389.
[54] J. Kim, D. Monllor-Satoca, W. Choi, Energy Environ. Sci. 5 (2012) 7647.
[55] B. Li, C. Lai, G. Zeng, D. Huang, L. Qin, M. Zhang, M. Cheng, X. Liu, H. Yi, C. Zhou, F. Huang, S. Liu, Y. Fu, Small 15 (2019) 1804565.
[56] G. Liu, J. Shi, F. Zhang, Z. Chen, J. Han, C. Ding, S. Chen, Z. Wang, H. Han, C. Li, Angew. Chem. Int. Ed. 53 (2014) 7295–7299.
[57] Y. Fu, L. Qin, D. Huang, G. Zeng, C. Lai, B. Li, J. He, H. Yi, M. Zhang, M. Cheng, X. Wen, Appl. Catal. B: Environ. 255 (2019) 117740.
[58] C. Lai, B. Li, M. Chen, G. Zeng, D. Huang, L. Qin, X. Liu, M. Cheng, J. Wan, C. Du, F. Huang, S. Liu, H. Yi, Int. J. Hydrogen Energy 43 (2018) 1749–1757.
[59] L. Li, C. Hu, L. Zhang, G. Yu, L. Lyu, F. Li, N. Jiang, J. Mater. Chem. A 7 (2019) 6946–6956.
[60] H. Wang, S. Chen, D. Yong, X. Zhang, S. Li, W. Shao, X. Sun, B. Pan, Y. Xie, J. Am. Chem. Soc. 139 (2017) 4737–4742.
[61] H. Wang, D. Yong, S. Chen, S. Jiang, X. Zhang, W. Shao, Q. Zhang, W. Yan, B. Pan, Y. Xie, J. Am. Chem. Soc. 140 (2018) 1760–1766.
[62] X. Sang, Y. Xie, M.W. Lin, M. Alhabeb, K.L. Van Aken, Y. Gogotsi, P.R.C. Kent, K. Xiao, R.R. Unocic, ACS Nano 10 (2016) 9193–9200.
[63] C. Lai, M. Zhang, B. Li, D. Huang, G. Zeng, L. Qin, X. Liu, H. Yi, M. Cheng, L. Li, Z. Chen, L. Chen, Chem. Eng. J. 358 (2019) 891–902.
[64] J. Ye, A. Hu, G. Ren, M. Chen, J. Tang, P. Zhang, S. Zhou, Z. He, Water Res. 134 (2018) 54–62.
[65] X. Liu, L. Huang, X. Wu, Z. Wang, G. Dong, C. Wang, Y. Liu, L. Wang, Chemosphere 210 (2018) 424–432.
[66] Y. Hu, K. Chen, Y.L. Li, J.Y. He, K.S. Zhang, T. Liu, W. Xu, X.J. Huang, L.T. Kong, J.H. Liu, Nanoscale 11 (2019) 1047–1057.